Quantitative X-ray phase-contrast computed tomography at 82 keV

Marian Willner, Martin Bech, Julia Herzen, Irene Zanette, Dieter Hahn, Johannes Kenntner, Juergen Mohr, Alexander Rack, Timm Weitkamp, Franz Pfeiffer

Quantitative X-ray phase-contrast computed tomography at 82 keV

Marian Willner,[1,*] Martin Bech,[1,2] Julia Herzen,[1,3] Irene Zanette,[1,4] Dieter Hahn,[1] Johannes Kenntner,[5] Juergen Mohr,[5] Alexander Rack,[4] Timm Weitkamp,[6] and Franz Pfeiffer[1]

[1] *Chair for Biomedical Physics, TU München, 85748 Garching, Germany*
[2] *Medical Radiation Physics, Lund University, 22100 Lund, Sweden*
[3] *Institute of Materials Science, Helmholtz-Zentrum Geesthacht, 21502 Geesthacht, Germany*
[4] *European Synchrotron Radiation Facility, 38043 Grenoble, France*
[5] *Karlsruhe Institute of Technology, 76344 Eggenstein-Leopoldshafen, Germany*
[6] *Synchrotron Soleil, 91192 Gif-sur-Yvette, France*

[*] *marian.willner@ph.tum.de*

Abstract: Potential applications of grating-based X-ray phase-contrast imaging are investigated in various fields due to its compatibility with laboratory X-ray sources. So far the method was mainly restricted to X-ray energies below 40 keV, which is too low to examine dense or thick objects, but a routine operation at higher energies is on the brink of realisation. In this study, imaging results obtained at 82 keV are presented. These comprise a test object consisting of well-defined materials for a quantitative analysis and a tooth to translate the findings to a biomedical sample. Measured linear attenuation coefficients μ and electron densities ρ_e are in good agreement with theoretical values. Improved contrast-to-noise ratios were found in phase contrast compared to attenuation contrast. The combination of both contrast modalities further enables to simultaneously assess information on density and composition of materials with effective atomic numbers $\tilde{Z} > 8$. In our biomedical example, we demonstrate the possibility to detect differences in mass density and calcium concentration within teeth.

OCIS codes: (110.7440) X-ray imaging; (110.6955) Tomographic imaging.

References and links

1. T. Weitkamp, A. Diaz, C. David, F. Pfeiffer, M. Stampanoni, P. Cloetens, and E. Ziegler, "X-ray phase imaging with a grating interferometer," Opt. Express **13**, 6296–6304 (2005).
2. A. Momose, "Recent advances in X-ray phase imaging," Jpn. J. Appl. Phys. **44**, 6355–6367 (2005).
3. F. Pfeiffer, T. Weitkamp, O. Bunk, and C. David, "Phase retrieval and differential phase-contrast imaging with low-brilliance X-ray sources," Nature Phys. **2**, 258–261 (2006).
4. F. Pfeiffer, C. Kottler, O. Bunk, and C. David, "Hard X-ray phase tomography with low-brilliance sources," Phys. Rev. Lett. **98**, 108105 (2007).
5. F. Pfeiffer, O. Bunk, C. David, M. Bech, G. Le Duc, A. Bravin, and P. Cloetens, "High-resolution brain tumor visualization using three-dimensional x-ray phase contrast tomography," Phys. Med. Biol. **52**, 6923–6930 (2007).
6. M. Bech, T. H. Jensen, R. Feidenhans'l, O. Bunk, C. David, and F. Pfeiffer, "Soft-tissue phase-contrast tomography with an X-ray tube source," Phys. Med. Biol. **54**, 2747–2753 (2009).
7. A. Momose, W. Yashiro, H. Maikusa, and Y. Takeda, "High-speed X-ray phase imaging and X-ray phase tomography with Talbot interferometer and white synchrotron radiation," Opt. Express **17**, 12540–12545 (2009).
8. T. Donath, F. Pfeiffer, O. Bunk, C. Grünzweig, E. Hempel, S. Popescu, P. Vock, and C. David, "Toward clinical X-ray phase-contrast CT: Demonstration of enhanced soft-tissue contrast in human specimen," Invest. Radiol. **45**, 445–452 (2010).

#182291 - $15.00 USD Received 3 Jan 2013; revised 25 Jan 2013; accepted 30 Jan 2013; published 11 Feb 2013

9. G. Schulz, T. Weitkamp, I. Zanette, F. Pfeiffer, F. Beckmann, C. David, S. Rutishauser, E. Reznikova, and B. Müller, "High-resolution tomographic imaging of a human cerebellum: comparison of absorption and grating-based phase contrast," J. R. Soc. Interface **7**, 1665–1676 (2010).
10. J. Herzen, T. Donath, F. Beckmann, M. Ogurreck, C. David, J. Mohr, F. Pfeiffer, and A. Schreyer, "X-ray grating interferometer for materials-science imaging at a low-coherent wiggler source," Rev. Sci. Instrum. **82**, 113711 (2011).
11. T. H. Jensen, A. Boettiger, M. Bech, I. Zanette, T. Weitkamp, S. Rutishauser, C. David, E. Reznikova, J. Mohr, L. B. Christensen, E. V. Olsen, R. Feidenhans'l, and F. Pfeiffer, "X-ray phase-contrast tomography of porcine fat and rind," Meat Sci. **88**, 379–383 (2011).
12. T. Thuering, P. Modregger, T. Grund, J. Kenntner, C. David, and M. Stampanoni, "High resolution, large field of view X-ray differential phase contrast imaging on a compact setup," Appl. Phys. Lett. **99**, 41111 (2011).
13. D. Stutman, T. J. Beck, J. A. Carrino, and C. O. Bingham, "Talbot phase-contrast X-ray imaging for the small joints of the hand," Phys. Med. Biol. **56**, 5697–5720 (2011).
14. M. Stampanoni, Z. Wang, T. Thuering, C. David, E. Roessl, M. Trippel, R. A. Kubik-Huch, G. Singer, M. K. Hohl, and N. Hauser, "The first analysis and clinical evaluation of native breast tissue using differential phase-contrast mammography," Invest. Radiol. **46**, 801–806 (2011).
15. A. Sztrókay, J. Herzen, S. D. Auweter, S. Liebhardt, D. Mayr, M. Willner, D. Hahn, I. Zanette, T. Weitkamp, K. Hellerhoff, F. Pfeiffer, M. F. Reiser, and F. Bamberg, "Assessment of grating-based X-ray phase-contrast CT for differentiation of invasive ductal carcinoma and ductal carcinoma in situ in an experimental ex vivo set-up," Eur. Radiol. **23**, 381–387 (2013).
16. A. Tapfer, M. Bech, A. Velroyen, J. Meiser, J. Mohr, M. Walter, J. Schulz, B. Pauwels, P. Bruyndonckx, X. Liu, A. Sasov, and F. Pfeiffer, "Experimental results from a preclinical X-ray phase-contrast CT scanner," Proc. Natl. Acad. Sci. USA **109**, 15691–15696 (2012).
17. T. Donath, F. Pfeiffer, O. Bunk, W. Groot, M. Bednarzik, C. Grünzweig, E. Hempel, S. Popescu, M. Hoheisel, and C. David, "Phase-contrast imaging and tomography at 60 keV using a conventional X-ray tube source," Rev. Sci. Instrum. **80**, 053701 (2009).
18. C. Kottler, V. Revol, R. Kaufmann, and C. Urban, "Dual energy phase contrast X-ray imaging with Talbot-Lau interferometer," J. Appl. Phys. **108**, 114906 (2010).
19. P. Bartl, F. Bayer, J. Durst, W. Haas, T. Michel, A. Ritter, T. Weber, and G. Anton, "Grating-based high energy X-ray interferometry with the Medipix-detector in simulation and measurement," J. Instrum. **5**, P10008 (2010).
20. J. Kenntner, V. Altapova, T. Grund, F. J. Pantenburg, J. Meiser, T. Baumbach, and J. Mohr, "Fabrication and characterization of analyzer gratings with high aspect ratios for phase contrast imaging using a Talbot interferometer," AIP Conf. Proc. **1437**, 89–93 (2012).
21. J. Herzen, T. Donath, F. Pfeiffer, O. Bunk, C. Padeste, F. Beckmann, A. Schreyer, and C. David, "Quantitative phase-contrast tomography of a liquid phantom using a conventional X-ray tube source," Opt. Express **17**, 10010–10018 (2009).
22. Z. Qi, J. Zambelli, N. Bevins, and G.-H. Chen, "Quantitative imaging of electron density and effective atomic number using phase contrast CT," Phys. Med. Biol. **55**, 2669–2677 (2010).
23. T. Weitkamp, I. Zanette, C. David, J. Baruchel, M. Bech, P. Bernard, H. Deyhle, T. Donath, J. Kenntner, S. Lang, J. Mohr, B. Müller, F. Pfeiffer, E. Reznikova, S. Rutishauser, G. Schulz, A. Tapfer, and J.-P. Valade, "Recent developments in X-ray Talbot interferometry at ESRF-ID19," Proc. SPIE **7804**, 780406 (2010).
24. I. Zanette, T. Weitkamp, S. Lang, M. Langer, J. Mohr, C. David, and J. Baruchel, "Quantitative phase and absorption tomography with an X-ray grating interferometer and synchrotron radiation," Phys. Status Solidi A **208**, 2526–2532 (2011).
25. E. C. McCullough, "Photon attenuation in computed tomography," Med. Phys. **2**, 307–320 (1975).
26. M. J. Berger, J. H. Hubbell, S. M. Seltzer, J. Chang, J. S. Coursey, R. Sukumar, D. S. Zucker, and K. Olsen, "XCOM: Photon Cross Section Database," (2010).
27. C. T. Chantler, K. Olsen, R. A. Dragoset, J. Chang, A. R. Kishore, S. A. Kotochigova, and D. S. Zucker, "X-Ray Form Factor, Attenuation and Scattering Tables," (2005).
28. M. d. P. Gutiérrez-Salazar and J. Reyes-Gasga, "Microhardness and chemical composition of human tooth," Mater. Res. **6**, 367–373 (2003).
29. S. M. Weidmann, J. A. Weatherell, and S. M. Hamm, "Variations of enamel density in sections of human teeth," Arch. Oral Biol. **12**, 85–97 (1967).
30. V. Coklica, F. Brudevold, and B. H. Amdur, "The distribution and composition of density fractions from human crown dentine," Arch. Oral Biol. **14**, 451–460 (1969).
31. A. Lange, M. P. Hentschel, A. Kupsch, and B. R. Müller, "Numerical correction of X-ray detector backlighting," Int. J. Mater. Res. **103**, 174–178 (2012).
32. X. Wu, H. Lu, and A. Yan, "X-ray phase-attenuation duality and phase retrieval," Opt. Lett. **30**, 379–381 (2005).

#182291 - $15.00 USD Received 3 Jan 2013; revised 25 Jan 2013; accepted 30 Jan 2013; published 11 Feb 2013

1. Introduction

In 2005, X-ray grating interferometry has been added to the portfolio of phase-contrast imaging techniques at synchrotron radiation facilities, exploiting the phase shift of X-rays in addition to their attenuation when traversing an object [1]. Especially the visualization of weakly absorbing materials profits from the high sensitivity that can be achieved with this complementary contrast mechanism [2]. The method has been extended from radiographic to tomographic imaging and successfully adapted to operate with laboratory X-ray sources shortly after [3, 4]. As a consequence of these developments, a broad use for medical applications, biological examinations, material characterization or food testing is meanwhile under investigation [5–16].

For studies of dense or thick objects high X-ray energies are required, but only few experiments with photon energies above 40 keV are reported in this context so far [17–19]. This is mainly attributed to the high demands on the gratings utilized in the interferometer. However, progress in the manufacturing process increasingly improves the grating performance at high energies [20].

Here, we demonstrate the feasibility of grating-based phase-contrast imaging at 82 keV and its potential to quantitatively assess information on material properties [21, 22]. The complementarity of both contrast modalities is discussed and image quality is compared in terms of contrast-to-noise ratios. Presented imaging results comprise a test object of known materials and a healthy molar tooth as biomedical sample. The measurements have been carried out at the beamline ID19 of the European Synchrotron Radiation Facility (ESRF), Grenoble, France.

2. Methods and materials

2.1. Grating-based phase-contrast imaging

For a detailed description of an X-ray grating interferometer similar to the one used in this work, we refer to the publication by Weitkamp et al. [1]. A phase grating is used as beam splitter and creates periodic intensity modulations at certain distances, the so-called fractional Talbot distances. Differences in the phase shift that X-rays undergo when passing two adjacent paths through an object cause a local shift of this pattern. Attenuation by the object, on the other hand, results in a loss of intensity as commonly exploited in conventional X-ray imaging.

Usually the detector pixel size exceeds the period of the intensity pattern, which typically is in the order of a few microns. For this reason, an analyzer grating of the same period as the interference pattern and with high absorbing structures is placed in front of the detector. This grating is translated perpendicularly to the grating lines while several images are acquired. During this stepping approach, a sinusoidal intensity oscillation is recorded in each detector pixel. Mean intensity and position of this curve can be evaluated by Fourier analysis. A comparison of data obtained with and without sample in the beam finally provides two radiographic images: the conventional attenuation-contrast and the differential phase-contrast image. The basic principle of the method is graphically displayed in Fig. 1 to give a more illustrative idea of the concept.

In a tomography scan, many projection images are generated from different angular directions and a 3D-volume of the object can then be reconstructed by applying, e.g., the filtered backprojection algorithm. In case of phase contrast, the filter function in the reconstruction algorithm has to be replaced by an imaginary Hilbert filter to cope with the differential nature of the projections [4]. Taking setup-dependent factors into consideration, the distribution of the linear attenuation coefficient $\mu(x,y,z)$ and the refractive index decrement $\delta(x,y,z)$ within the sample can be determined from the attenuation-contrast and phase-contrast datasets, respectively [21].

A crucial requirement to properly resolve the position of the intensity pattern and, thus, to

#182291 - $15.00 USD Received 3 Jan 2013; revised 25 Jan 2013; accepted 30 Jan 2013; published 11 Feb 2013

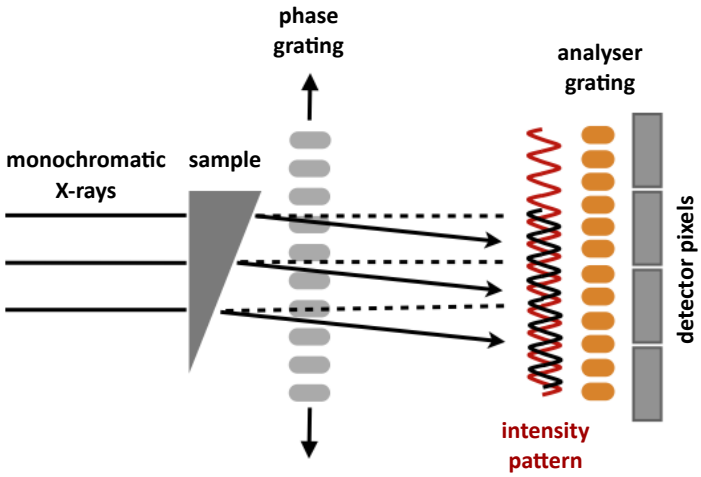

Fig. 1. Principle of a grating-based X-ray interferometer. The phase grating creates a periodic intensity pattern that can be resolved by placing an analyzer grating in front of the detector. A sample in the incident beam causes slight refraction, which results in a local shift of the analyzed pattern.

attain good phase-contrast image quality, is a high absorbance of the analyzer grating structures. For analyzer gratings made of gold, heights of 100 μm or more are needed for energies above 40 keV. In combination with the small periods of a couple of microns, the manufacturing of gratings with aspect-ratios of 100 to 150 is still challenging. However, advances in the fabrication process are ongoing and routine application of grating-based phase-contrast imaging at high energies might become available soon [20].

2.2. Samples and measurements

The measurements for the assessment of the feasibility at 82 keV have been carried out at the beamline ID19 of the European Synchrotron Radiation Facility (ESRF) in Grenoble, France. An analyzer grating with a period of 2.4 μm and gold structures of 100 μm height has been produced at the Karlsruhe Institute of Technology (KIT), Karlsruhe, Germany. At 82 keV, directly above the absorption edge of gold, the transmission through the grating bars is of only 20 % which guarantees a well-functioning interferometer. The height of the employed nickel phase grating was 14.1 μm, introducing an approximate phase shift of $\pi/2$ to the incoming photons of 82 keV. Since the measurements were performed with parallel beam, the period of the phase grating is equal to the period of the analyzer grating (2.4 μm). The distance between the two gratings was 19.8 cm which corresponds to the first fractional Talbot distance.

The whole setup was located 150 m away from the wiggler source with a horizontal size of about 120 μm, providing a high degree of transverse coherence and a maximum beam size at sample position of 40 mm (width) by 15 mm (height) [23]. A FReLon CCD (type e2v, 2048x2048 pixels), lens-coupled to a GadOx scintillator of 10 μm thickness, has been used as detector. The optics have been set to an effective pixel size of 8 μm. The beam height was limited to 550 detector pixels (corresponding to 4.4 mm) due to the finite length of the monochromator crystals and their inclination. The photon flux density at the sample position was approximately 10^{10} photons/s/0.1%bw/mm^2. The visibility had a value of 26 % in the experiments. This important performance factor characterizes the ability of the interferometer to resolve the intensity pattern created by the phase grating. Typical visibility values range from

#182291 - $15.00 USD Received 3 Jan 2013; revised 25 Jan 2013; accepted 30 Jan 2013; published 11 Feb 2013

10-15 % at laboratory X-ray tube setups [8,16] to 40 % at lower energy synchrotron radiation [1] depending on the setup parameters.

A test object consisting of six rods - PMMA, PVC, PTFE, glass, aluminum (Al) and titanium (Ti) - with 2 mm diameter each has been designed. The mass densities of the materials range from $1.19\,g/cm^3$ (PMMA) to $4.5\,g/cm^3$ (Ti) and the covered elements yield atomic numbers up to $Z = 22$ (Ti). The rods were placed in a tube filled with water to avoid phase wrapping caused by strong differences in phase shift between rods and air which can affect the quantitativeness of the measurements [24].

The sample was installed upstream of the phase grating and a tomography scan with 799 projections over 360 degrees has been performed in a total scanning time of 2 hours. Four images have been acquired per projection and every 100 projections 10 flat fields (stepping scans without object) have been recorded. The detector pixels were binned 2x2 resulting in a voxel size of 16^3 μm^3 for the reconstructed dataset.

A healthy molar tooth donated by one of the authors has been taken as biomedical sample. It was put in a tube filled with ethanol and scanned with 999 projections over 360 degrees and without detector binning. All other parameters were identical to the tomography scan of the test object.

2.3. X-ray interactions and implied information content

Phase contrast gives the distribution of the refractive index decrement $\delta(x,y,z)$ within the object, which is given by

$$\delta = \frac{r_0 h^2 c^2}{2\pi E^2} \sum N_i f_i^1, \tag{1}$$

where r_0 is the classical electron radius, h is the Planck constant, c is the speed of light, N_i is the atomic density of type i atoms (number of atoms per unit volume) and f_i^1 is the real part of their atomic scattering factor in the forward direction [21]. In absence of any absorption edges f_i^1 can be replaced by the element's atomic number Z_i and the sum $\sum N_i f_i^1$ reflects the electron density ρ_e of the material. At 82 keV this is valid for all elements with $Z < 79$. Thus, phase-contrast imaging allows for direct access to the electron density distribution

$$\rho_e(x,y,z) = \frac{2\pi E^2}{r_0 h^2 c^2} \cdot \delta(x,y,z). \tag{2}$$

If the mass electron density N_g (number of electrons per unit mass) of a material is known, the electron density ρ_e can be further used to evaluate the corresponding mass density ρ according to

$$\rho = \rho_e / N_g. \tag{3}$$

For most elements except of hydrogen and heavy elements, the mass electron density can be approximated by $N_A/2$ in electrons/g, where N_A is the Avogadro constant without physical dimension [25]. Especially in case of compounds containing several elements but only small amounts of hydrogen, N_g is nearly independent of the actual material composition. This is exemplarily made use of in a quantitative analysis of the imaging results of the tooth later.

Attenuation contrast delivers the linear attenuation coefficient $\mu(x,y,z)$ of every voxel within the object. It originates from the three types of photon interactions - photoelectric absorption [ph], (incoherent) Compton scattering [incoh] and (coherent) Raleigh scattering [coh] - and can be expressed by

$$\mu = \mu_{incoh} + \mu_{ph} + \mu_{coh} = \rho_e \cdot \left(\sigma^e_{incoh}(E) + \sigma^e_{ph}\left(E, \tilde{Z}_{ph}\right) + \sigma^e_{coh}\left(E, \tilde{Z}_{coh}\right)\right) \tag{4}$$

#182291 - $15.00 USD Received 3 Jan 2013; revised 25 Jan 2013; accepted 30 Jan 2013; published 11 Feb 2013

with the electron density ρ_e and the electronic cross-sections for Compton scattering σ^e_{incoh}, photoelectric absorption σ^e_{ph} and Raleigh scattering σ^e_{coh} [25]. The Compton scattering cross-section $\sigma^e_{incoh}(E)$ is approximately the Klein-Nishina cross-section $\sigma_{kn}(E)$ and only dependent on the photon energy E. The approximation of the electronic cross-section for photoelectric absorption

$$\sigma^e_{ph}\left(E,\tilde{Z}_{ph}\right) = C_1 \frac{\tilde{Z}^k_{ph}}{E^l} \tag{5}$$

and the electronic cross-section for Raleigh scattering

$$\sigma^e_{coh}\left(E,\tilde{Z}_{coh}\right) = C_1 \frac{\tilde{Z}^m_{coh}}{E^n} \tag{6}$$

show an additional dependency on material specific effective atomic numbers

$$\tilde{Z}_{ph} = \left(\sum \alpha_i Z_i^k\right)^{1/k} \quad \text{and} \quad \tilde{Z}_{coh} = \left(\sum \alpha_i Z_i^m\right)^{1/m}, \tag{7}$$

where α_i is the electron fraction of the ith element with atomic number Z_i present in the material. The numbers k and m are around 3.8 and 2.0, respectively, but vary slightly depending on the photon energy and on the composition of the material [25].

Referring to Eqs. (5) and (6), the energy dependencies ($l \approx 3$ and $n \approx 2$) exhibit the decreasing influence of photoelectric absorption and coherent scattering on the linear attenuation coefficient μ with increasing energy. If the attenuation process is purely caused by Compton scattering, the signal in attenuation contrast is proportional to the electron density ρ_e as it is in phase conrast. Otherwise, the linear attenuation coefficient μ yields information on density and material composition. In this case, the information content provided by phase contrast and attenuation contrast is complementary.

Qi et al. have demonstrated the possibility to assign an effective atomic number to a material by combining both contrast mechanisms [22]. In this study, we introduce an alternative approach to reveal the composition information existing in the linear attenuation coefficient μ. Equations (5) and (6) indicate the increasing contribution of photoelectric absorption and coherent scattering to the linear attenuation coefficient μ with increasing effective atomic number at a given energy. Conversely, the ratio of Compton scattering to the linear attenuation coefficient μ diminish. The latter can be determined by exploiting both contrast modalities

$$\frac{\mu_{incoh}}{\mu} \approx \frac{\rho_e \sigma_{kn}}{\mu}, \tag{8}$$

where ρ_e and μ are gained from the phase- and attenuation-contrast measurements and σ_{kn} can be calculated for the relevant energy. The Compton scattering ratios of single elements with atomic numbers Z can be obtained from their tabulated total attenuation cross-sections $\sigma_{tot}(Z)$:

$$\frac{\mu_{incoh}}{\mu} \approx \frac{\rho_e \sigma_{kn}}{\rho_e \sigma^e_{tot}} = \frac{\sigma_{kn}}{\sigma_{tot}(Z)/Z}. \tag{9}$$

Following Eqs. (8) and (9), a comparison of measurement results to theoretical values allows for a rough estimation of the effective atomic number $\tilde{Z}$ attributed to a material. If the contribution of coherent scattering is small compared to photoelectric absorption, the identified effective atomic number $\tilde{Z}$ corresponds to $\tilde{Z}_{ph}$ as defined in Eq. (7). This new approach is applied to the test object and tooth data.

All theoretical values stated in this paper are based on tabulated data from the National Institute of Standards and Technology (NIST) [26, 27]. Contrast-to-noise ratios for the comparison

#182291 - $15.00 USD Received 3 Jan 2013; revised 25 Jan 2013; accepted 30 Jan 2013; published 11 Feb 2013

of the relative contrast between different materials in the two image modalities are calculated by

$$CNR = \frac{|S_A - S_B|}{\sqrt{\sigma_A^2 + \sigma_B^2}}, \tag{10}$$

with $S_{A,B}$ being the mean values of the respective signal in selected regions-of-interest for material A and B and $\sigma_{A,B}$ being the associated standard deviations.

3. Results

3.1. Test object: imaging and analysis results

The imaging results of the test object displaying both attenuation and phase contrast are shown in Fig. 2. The highest signal in both modalities is obtained for titanium, which has the largest mass density of all involved materials as well as the highest atomic number Z. On the contrary, PMMA yields the lowest signal and is hardly distinguishable from the surrounding water in attenuation contrast.

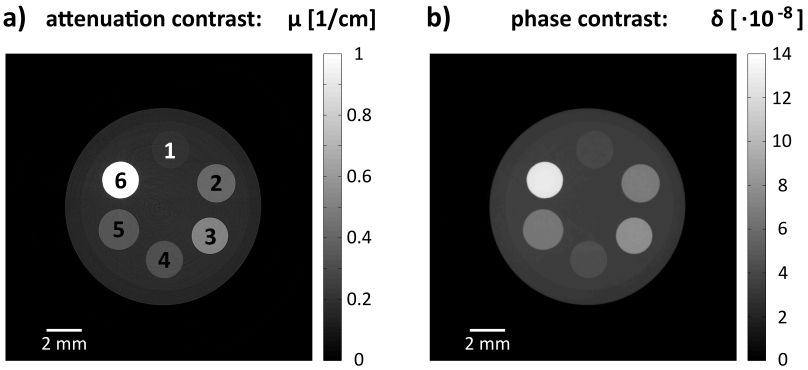

Fig. 2. Imaging results. Attenuation contrast (a) and phase contrast (b) of a test object consisting of PMMA (1), glass (2), aluminum (3), PVC (4), PTFE (5) and titanium (6).

Linear attenuation coefficients μ, refractive index decrements δ and electron densities ρ_e have been determined by regions-of-interest analysis comprising 50x50x50 voxels for each material. The mean values and associated standard deviations can be found together with theoretical values in Table 1. The theoretical values are all within one standard deviation of the values evaluated from the measurements except in case of the linear attenuation coefficient μ of titanium.

3.2. Comparison of attenuation and phase contrast

The linear attenuation coefficients μ are plotted versus the corresponding electron densities ρ_e with error bars indicating the standard deviations in Fig. 3. In addition, the linear attenuation coefficient for Compton scattering $\mu_{incoh} = \rho_e \sigma_{kn}$ is drawn in the graph.

With the markers of PMMA and PTFE almost lying on that line, one can assume that for these materials the attenuation process is dominated by incoherent scattering. In both contrast modalities their signals are more or less proportional to their electron densities and no complementary information is given. However, an improved contrast-to-noise ratio of 16.52 in phase contrast compared to 2.34 in attenuation contrast could be found. The material pairs PMMA/PVC and PTFE/glass have only small density differences and with factors of 1.22 and 1.3, respectively,

#182291 - $15.00 USD Received 3 Jan 2013; revised 25 Jan 2013; accepted 30 Jan 2013; published 11 Feb 2013

Table 1. Properties and quantitative analysis results of the materials used in the test object. Linear attenuation coefficients μ are obtained from attenuation contrast; refractive index decrements δ and electron densities ρ_e are extracted from phase contrast. Theoretical values (theo) are based on NIST databases and material compositions.

material	composition	ρ $\left[\frac{g}{cm^3}\right]$	μ $\left[\frac{1}{cm}\right]$	μ_{theo} $\left[\frac{1}{cm}\right]$	δ $\left[\cdot 10^{-8}\right]$	δ_{theo} $\left[\cdot 10^{-8}\right]$	ρ_e $\left[\frac{10^{29}}{m^3}\right]$	$\rho_{e,theo}$ $\left[\frac{10^{29}}{m^3}\right]$
PMMA	$C_5H_8O_2$	1.19	0.207 $\pm$0.041	0.207	3.96 $\pm$0.10	3.96	3.87 $\pm$0.10	3.87
PVC	C_2H_3Cl	1.4	0.321 $\pm$0.043	0.314	4.35 $\pm$0.13	4.43	4.25 $\pm$0.13	4.32
PTFE	C_2F_4	2.2	0.344 $\pm$0.042	0.356	6.55 $\pm$0.12	6.52	6.39 $\pm$0.11	6.36
glass	SiO_2	2.2	0.410 $\pm$0.041	0.419	6.80 $\pm$0.13	6.79	6.63 $\pm$0.12	6.63
aluminum	97% Al, 3% Mg	2.67	0.516 $\pm$0.041	0.527	7.88 $\pm$0.11	7.95	7.69 $\pm$0.11	7.76
titanium	>99.6%	4.5	1.674 $\pm$0.048	1.738	12.78 $\pm$0.11	12.79	12.46 $\pm$0.11	12.47

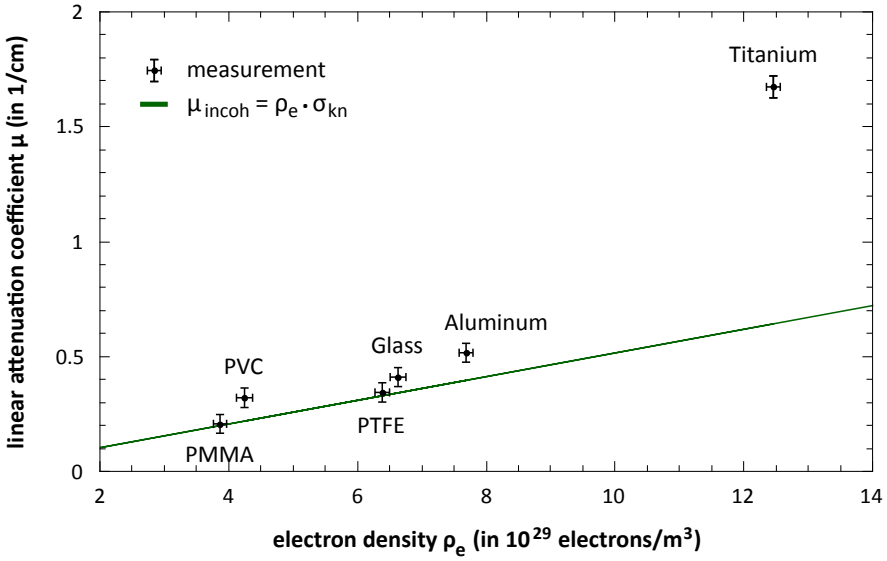

Fig. 3. Measured linear attenuation coefficients μ versus corresponding electron densities ρ_e. Standard deviations are indicated by error bars and the solid green line represents the linear attenuation coefficient for Compton scattering μ_{incoh}.

they have the lowest contrast gain by phase-contrast imaging. The biggest benefit, a factor of 32.8, is achieved for the discrimination of PVC and PTFE, which exhibit almost the same linear attenuation coefficients μ despite large differences in density. Contrast-to-noise ratios for a selection of material combinations are quoted in Table 2.

#182291 - $15.00 USD Received 3 Jan 2013; revised 25 Jan 2013; accepted 30 Jan 2013; published 11 Feb 2013

Table 2. Contrast-to-noise ratios in phase contrast CNR_{ph} and attenuation contrast CNR_{att} for selected material combinations. A contrast gain by phase-contrast imaging can be noticed in all cases.

material	CNR_{ph}	CNR_{att}	CNR_{ph}/CNR_{att}
PTFE - glass	1.47	1.13	1.3
PMMA - PVC	2.35	1.93	1.22
PVC - PTFE	12.68	0.39	32.79
PVC - glass	13.61	1.52	8.98
PMMA - PTFE	16.52	2.34	7.07
PVC - aluminum	20.86	3.31	6.3
aluminum - titanium	31.45	18.35	1.71
PMMA - titanium	57.99	23.35	2.48

3.3. Evaluation of effective atomic numbers $\tilde{Z}$

The linear attenuation coefficients μ of PVC, glass, aluminum and titanium are not mainly made up of Compton scattering, but the photoelectric effect (and coherent scattering) plays a role in the attenuation process as well. We want to exploit this fact to get additional information on the composition of these materials. The ratio of incoherent scattering to the linear attenuation coefficient of single elements $\sigma_{kn}/(\sigma_{tot}/Z)$ decreases with higher atomic numbers Z as illustrated for $Z =$ 1-26 in Fig. 4.

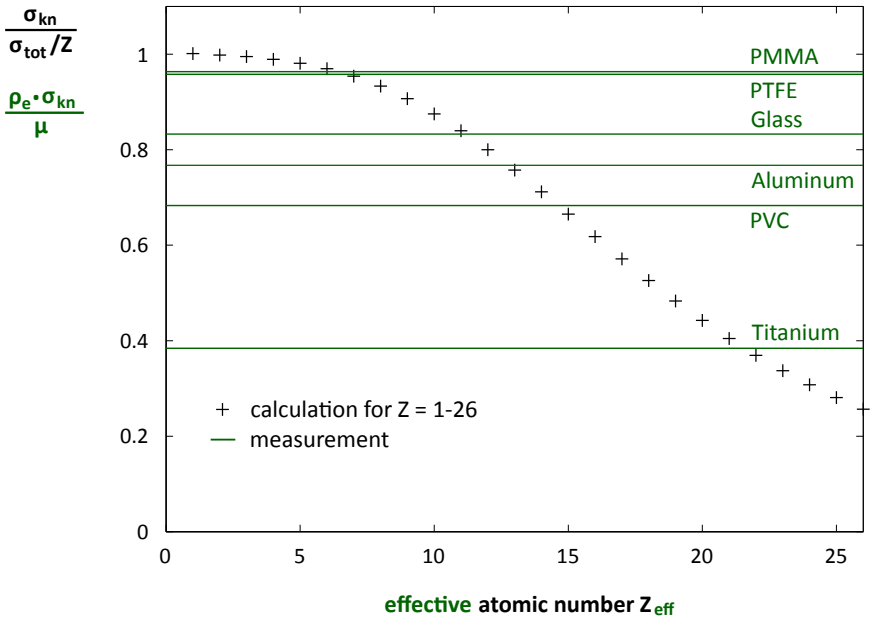

Fig. 4. The ratio of Compton scattering to the linear attenuation coefficient μ_{incoh}/μ of single elements decreases with atomic number Z as illustrated by the black markers. The combination of attenuation and phase contrast allows to determine the contribution of Compton scattering to the attenuation process within a material (solid green lines) and, thus, to draw conclusions on its effective atomic number $\tilde{Z}$.

#182291 - $15.00 USD Received 3 Jan 2013; revised 25 Jan 2013; accepted 30 Jan 2013; published 11 Feb 2013

The green lines represent the ratios $\rho_e \sigma_{kn}/\mu$ obtained for the materials of the test object in the measurement. Aluminum and titanium are close to the values corresponding to their theoretical atomic numbers $Z = 13$ and $Z = 22$, respectively. The small deviations can be explained by the underestimation of the linear attenuation coefficients μ in the measurements. The aluminum rod contains also a few percent of magnesium ($Z = 12$). The effective atomic numbers determined for PMMA ($C_5H_8O_2$) and PTFE (C_2F_4) are between $\tilde{Z} = 6$ and $\tilde{Z} = 7$. However, the ratio of Compton scattering amounts to approximately 95 % in both cases and in this domain little changes in value have a large impact on the identified effective atomic number $\tilde{Z}$. PVC (C_2H_3Cl) has a relatively high effective atomic number between $\tilde{Z} = 14$ and $\tilde{Z} = 15$, which can be traced back to the content of chlorine ($Z = 17$).

PVC and PTFE have very similar linear attenuation coefficients μ, but different material properties can be assigned to the materials by combining both contrast modalities: a low density and the presence of heavier elements in case of PVC compared to a higher density but lighter elements in case of PTFE.

As noted in connection with PMMA and PTFE, at 82 keV the linear attenuation coefficients μ of low Z materials are mostly attributed to Compton scattering and no reliable effective atomic numbers $\tilde{Z}$ can be ascertained. However, for materials with effective atomic numbers of $\tilde{Z} > 8$, attenuation and phase contrast deliver complementary information and conclusions on density and material composition can be drawn.

3.4. Tooth: imaging and analysis results

With regard to the human body, the last statement applies in particular to bones and teeth due to the high content of calcium ($Z = 20$). For this reason a molar tooth has been chosen as biomedical sample. The imaging results are displayed in Fig. 5. The two main components, enamel and dentin, are well discriminable in both contrast modes. The contrast-to-noise ratio of the two mineralized tissues is around 2 in attenuation contrast and ranges from 10 to 14 in phase contrast.

To evaluate the potential of a quantitative material characterization, the mass densities ρ and effective atomic numbers $\tilde{Z}$ have been determined at 50 positions in enamel and 20 positions in dentin. Each region-of-interest covered 20x20x20 voxels (of 8^3 μm^3) corresponding to a physical size of $4.1 \cdot 10^{-3}$ mm^3. The results thereof are presented in Fig. 5. The electron mass densities N_g used for the conversion of electron densities to mass densities according to Eq. (3) have been calculated based on tissue compositions presented by Gutierrez-Salazar [28]. In spite of significant differences in composition – e.g. 32 % carbon and 18 % calcium in enamel versus 52 % carbon and 9 % calcium in dentin – the electron mass densities N_g are almost identical and account for $2.994 \cdot 10^{23}$ and $2.999 \cdot 10^{23}$ electrons/g, respectively.

A mass density of enamel between 2.85 g/cm^3 and 3.00 g/cm^3 is reported in literature [29] which is in very good agreement to our analysis. The detected mass densities for dentin are lower than those of enamel and with 2.15 to 2.22 g/cm^3 as well in the range of previous findings of 2.1 to 2.3 g/cm^3 [30]. As the noise within the single analyzed ROIs was 0.04-0.045 g/cm^3 and the error of the determined mass densities is even smaller, one can assume that the observed mass density distributions of enamel (Fig. 5c) and dentin (Fig. 5d) reflect inhomogeneities within the corresponding material.

The effective atomic numbers $\tilde{Z}$ evaluated in our examination are between 15 and 16 for enamel and between 13 and 14.5 for dentin (Fig. 5e). The greater values obtained for enamel represent the higher content of calcium and phosphorus in enamel than in dentin [28]. To what extent small differences in composition within each component can be distinguished from statistical measurement uncertainties has to be clarified in a more comprehensive study on this topic.

#182291 - $15.00 USD Received 3 Jan 2013; revised 25 Jan 2013; accepted 30 Jan 2013; published 11 Feb 2013

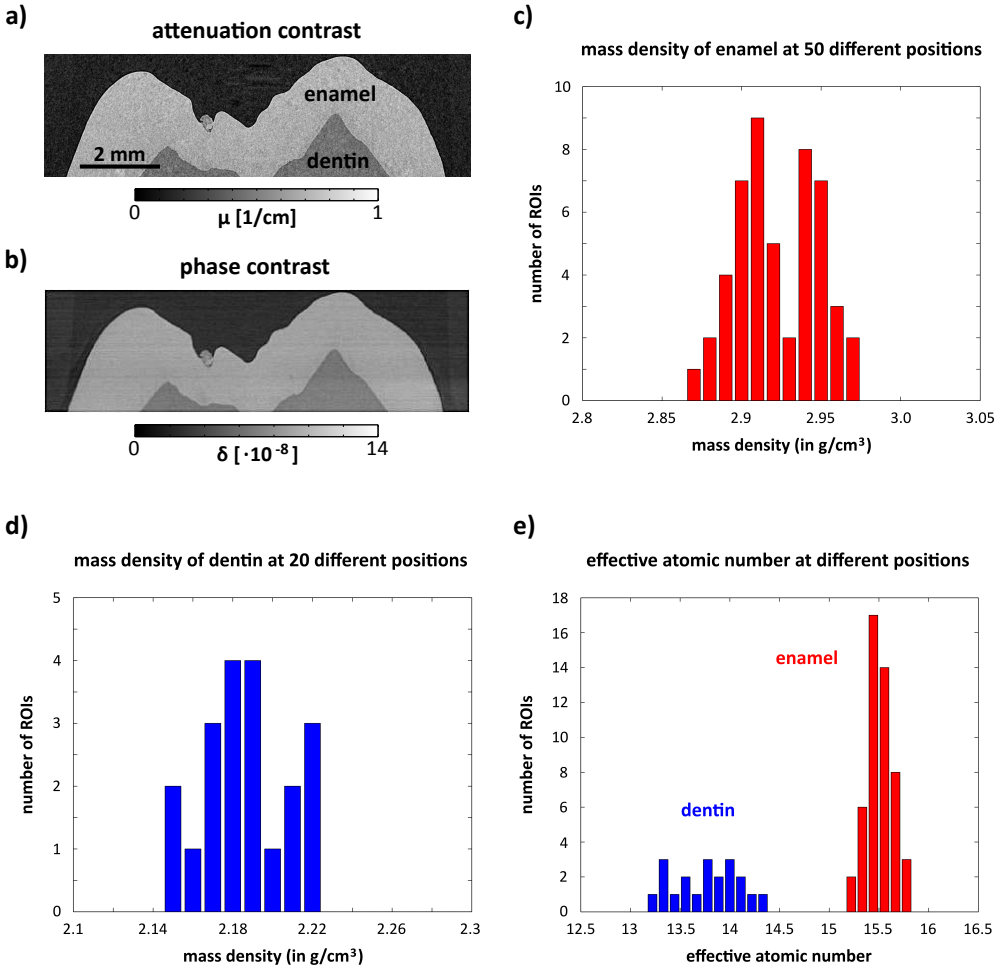

Fig. 5. Attenuation-contrast (a) and phase-contrast (b) imaging results of a tooth. Mass densities ρ evaluated at 50 positions in enamel and 20 positions in dentin are presented in (c) and (d), respectively. Effective atomic numbers $\tilde{Z}$ obtained by exploiting both contrast modalities are displayed in (e).

4. Conclusion

We successfully demonstrated the feasibility of quantitative grating-based phase-contrast imaging at 82 keV. A tomography scan of a self-built test object has been performed to quantitatively assess information on material properties. In phase contrast, the evaluated refractive index decrements δ and electron densities ρ_e of the six employed materials have been determined within an error range of 2 % of the corresponding theoretical values. The measured linear attenuation coefficients μ in attenuation contrast show a good agreement as well, but are slightly underestimated in most cases. Possible causes for the discrepancy may be X-ray fluorescence scattering by the analyzer grating or detector backlighting [31], which have not been considered within our study. More detailed investigations concerning this issue are needed.

In addition, the combination of both contrast modalities allows to determine the contribution of Compton scattering to the linear attenuation coefficient μ. This information can be used to

#182291 - $15.00 USD Received 3 Jan 2013; revised 25 Jan 2013; accepted 30 Jan 2013; published 11 Feb 2013

assign effective atomic numbers $\tilde{Z}$ to the materials and, thus, draw conclusions on their elemental compositions. A good example for the added value of phase contrast is the discrimination of PVC and PTFE. Both materials show a very similar linear attenuation coefficient μ in attenuation contrast. Taking into account the supplementary information attained by phase-contrast imaging, a low density and the presence of heavier elements can be observed for PVC compared to the denser PTFE, which contains solely light elements.

Moreover, we have shown the possibility to simultaneously identify mass densities and different tissue compositions within a tooth. Please note that these examinations have been performed for the purpose of demonstrating the translation of the previous results to a potential biomedical application. If the method is valuable and sensitive enough to address open questions in dental research further evaluation is required.

Compton scattering is the dominating attenuation process at 82 keV for materials with low effective atomic numbers ($\tilde{Z} \leq 8$), which include most biological soft tissues. In these cases, the signal of both modalities - attenuation and phase contrast - is then proportional to the electron density. Phase-contrast imaging can benefit from this phase-attenuation duality, e.g., when it comes to phase-retrieval using in-line holography [32]. On the other hand, it constitutes a severe limitation as complementarity is lost and the advantage of phase-contrast imaging is restricted to an enhancement of image quality. In our measurements this applies to the materials PMMA and PTFE, for which we could observe a contrast gain by a factor of 7 in the phase-contrast images. To what extent the achieved improvement can be realized at conventional X-ray tubes will be a crucial aspect for a broad application in diagnostic imaging of soft tissues when moving towards energies around 80 keV. In this energy regime, the method is in particular promising for the characterization of materials with effective atomic numbers $\tilde{Z} > 8$ as it provides separate information on their density and composition.

Acknowledgments

We acknowledge financial support through the DFG Cluster of Excellence Munich-Centre for Advanced Photonics (MAP), the DFG Gottfried Wilhelm Leibniz program and the European Research Council (ERC, FP7, StG 240142). This work was carried out with the support of the Karlsruhe Nano Micro Facility (KNMF, www.kit.edu/knmf), a Helmholtz Research Infrastructure at Karlsruhe Institute of Technology (KIT). Timm Weitkamp acknowledges support from the French research networks RTRA "Digiteo" and RTRA "Triangle de la Physique" (grants 2009-034T and 2009-79D).

#182291 - $15.00 USD Received 3 Jan 2013; revised 25 Jan 2013; accepted 30 Jan 2013; published 11 Feb 2013